J Geod (2008) 82:637–653
DOI 10.1007/s00190-008-0219-8

ORIGINAL ARTICLE

A comparison of different mass elements for use in gravity gradiometry

F. Wild-Pfeiffer

Received: 28 March 2006 / Accepted: 22 January 2008 / Published online: 3 April 2008

Abstract Topographic and isostatic mass anomalies affect the external gravity field of the Earth. Therefore, these effects also exist in the gravity gradients observed, e.g., by the satellite gravity gradiometry mission GOCE (*G*ravity and Steady-State *O*cean *C*irculation *E*xperiment). The downward continuation of the gravitational signals is rather difficult because of the high-frequency behaviour of the combined topographic and isostatic effects. Thus, it is preferable to smooth the gravity field by some topographic-isostatic reduction. In this paper the focus is on the modelling of masses in the space domain, which can be subdivided into different mass elements and evaluated with analytical, semi-analytical and numerical methods. Five alternative mass elements are reviewed and discussed: the tesseroid, the point mass, the prism, the mass layer and the mass line. The formulae for the potential, the attraction components and the Marussi tensor of second-order potential derivatives are provided. The formulae for different mass elements and computation methods are checked by assuming a synthetic topography of constant height over a spherical cap and the position of the computation point on the polar axis. For this special situation an exact analytical solution for the tesseroid exists and a comparison between the analytical solution of a spherical cap and the modelling of different mass elements is possible. A comparison of the computation times shows that modelling by tesseroids with different methods produces the most accurate results in an acceptable computation time. As a numerical example, the Marussi tensor of the topographic effect is computed globally using tesseroids calculated by Gauss–Legendre cubature (3D) on the basis of a digital height model. The order of magnitude in the radial-radial component is about ±8 E.U.

Keywords Topographic reductions · Isostatic reductions · Mass elements (tesseroid, prism, point mass, mass layer, mass line) · Satellite gravity gradiometry

Electronic supplementary material The online version of this article (doi:10.1007/s00190-008-0219-8) contains supplementary material, which is available to authorized users.

F. Wild-Pfeiffer (✉)
Institute of Navigation, University of Stuttgart,
Breitscheidstr. 2, 70174 Stuttgart, Germany
e-mail: wild-pfeiffer@nav.uni-stuttgart.de

1 Introduction

Gravity gradiometry is strongly sensitive to the gravity field of the Earth induced by the topographic and isostatic masses. Because of the rough gravity field the downward continuation is rather complex and challenging. Using a topographic-isostatic reduction based on different isostatic and condensation models is one possibility to smooth the *S*atellite *G*ravity *G*radiometry (SGG) data (e.g. Heck and Wild 2005; Makhloof and Ilk 2005; Janák et al. 2007; Wild-Pfeiffer 2007). Another possibility to obtain a smooth gravity field is the remove-compute-restore (RCR) technique (Forsberg and Tscherning 1997). In this procedure, as well as in many other geodetic applications such as computation of a quasigeoid (Denker 2006), the modelling of the topographic masses is required, which generally are subdivided into mass elements of simple geometrical shape. By modelling the topographic masses, it is possible to differentiate between mass elements that are related to Cartesian, ellipsoidal or spherical coordinates, depending on the location (near zone, far zone) with respect to the computation point. The most common mass element for the immediate vicinity of the computation point, in which the topography is mostly described in Cartesian coordinates, is the rectangular prism

as analyzed, for example, by Mader (1951); Nagy (1966); Forsberg (1984); Tsoulis (1999) and Nagy et al. (2000, 2002). Because of the time-consuming computation of the gravity field of a prism, some alternative mass elements like the tesseroid (Heck and Seitz 2007), the point mass, the mass line and the mass layer (e.g. Grüninger 1990; Kuhn 2000) or a radial integration of the volume elements and a numerical solution of the resulting 2D-integral (e.g. Martinec 1998; Novák et al. 2001) can be used for the topographic reduction. The point mass, mass line and mass layer approximations are mostly applied in the modelling of the far zone, while the tesseroid is used in the near zone.

The main purpose of the paper is a systematic and consistent review of the gravitational effects of these mass elements on the potential and its first and, in particular, second-order derivatives for use in terrestrial and satellite-based gravity field modelling. In Sect. 2 analytical, semi-analytical and numerical solutions of the respective integrals are discussed and the effect of the topographic masses is described. Finally, in Sect. 3 the numerical properties of various methods of mass modelling are analyzed with respect to accuracy and computation time, considering a simple synthetic topography of constant height over a spherical cap centered at the computation point. A numerical example is presented, modelling the global topographic effect.

2 Gravitational effect of masses

To describe the gravitational effect of the topographic or isostatic masses the geoid is approximated by a sphere Σ_g of radius R. The spherical approximation will yield sufficient results in most cases (Novák and Grafarend 2005). The radius of the computation point Q is denoted by r, the surface point P' has the geocentric radius r', and r_p is the radius of the point P that is situated below Q and on the Earth's surface; ψ is the distance between the radius vectors of Q and P' (Fig. 1).

The potential of the masses can be described by the Newton integral in spherical coordinates (e.g. Blakely 1995)

$$V(Q) = G \iiint_{\Omega} \frac{\rho}{\ell} \, \mathrm{d}\Omega, \tag{1}$$

$$\ell = \sqrt{r^2 + \xi^2 - 2r\xi \cos\psi}, \tag{2a}$$

$$\cos\psi = \sin\varphi \sin\varphi' + \cos\varphi \cos\varphi' \cos\left(\lambda - \lambda'\right), \tag{2b}$$

where (r, ϕ, λ) and (ξ, ϕ', λ') denote the spherical coordinates of the computation point and the variable integration point, respectively, related to a terrestrial reference frame. G is the gravitational constant, ρ the local mass density and $\mathrm{d}\Omega = \xi^2 \mathrm{d}\xi \mathrm{d}\sigma$ the volume element ($\mathrm{d}\sigma$ is the surface element of the unit sphere). To discretize the masses, a segmentation into volume elements Ω_i is made where the density ρ_i is assumed to be constant:

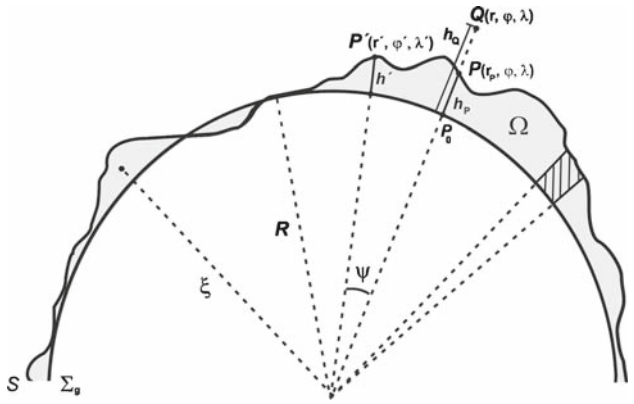

Fig. 1 Geometry of the topography in spherical approximation

$$V(Q) = G \sum_i \rho_i \iiint_{\Omega_i} \frac{\mathrm{d}\Omega}{\ell}. \tag{3}$$

The triple integral of each volume element is analytically solvable for the prism (see Sect. 2.2), the point mass (see Sect. 2.3), the mass line (see Sect. 2.4) and the mass layer (see Sect. 2.5). In case of the tesseroid, no analytical solution exists in general (see Sect. 2.1); one variant to solve the triple integral is the evaluation by pure numerical methods, e.g. the Gauss–Legendre cubature (3D). A second alternative is provided by a Taylor series expansion of the integrand, where the term of zero-order is equivalent to the point mass formula (see Sect. 2.3). Another possibility to compute the elliptic integral is the decomposition into a one-dimensional integral over the radial parameter ξ for which an analytical solution exists and a 2D spherical integral which is solved by quadrature methods, especially the Gauss–Legendre cubature (2D). The approximation of the tesseroids by prisms (see Sect. 2.2) by postulating mass conservation also provides an option for the solution of the triple integral; this procedure requires a transformation of the coordinate system of the prism into the coordinate system of the computation point.

The gravitational potential of the topographic masses can be described analogously with the Newton integral in spherical coordinates Eq. (1)

$$V_t(Q) = G \iint_{\sigma} \left[\int_{\xi=R}^{\xi=R+h'(\lambda',\varphi')} \frac{\rho}{\ell} \xi^2 \mathrm{d}\xi \right] \mathrm{d}\Omega. \tag{4}$$

The masses are discretized into volume elements Ω_i (see Sects. 2.1–2.5) and the overall effect of the masses is determined by a summation [Eq. (3)]. The segmentation into volume elements and the subsequent summation can also be applied in the RTM (Residual Terrain Modelling) method.

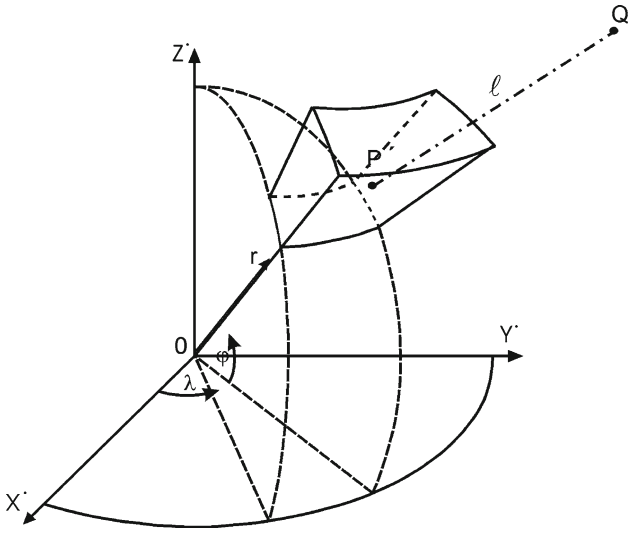

Fig. 2 Tesseroid in the global coordinate system

2.1 Tesseroid

The tesseroid is a mass element (e.g., Anderson 1976; Grüninger 1990; Kuhn 2000; Heck and Seitz 2007) that is bounded by two concentric spheres (r_1 = const., r_2 = const.), two meridian planes (λ_1 = const., λ_2 = const.) and two conical surfaces whose engendering lines go through the centre of the sphere and along the parallels ϕ_1 = const., ϕ_2 = const. (see Fig. 2).

2.1.1 Triple integral representation and numerical integration of 3D integrals

The potential of a tesseroid can be described with Newton's integral [Eq. (1)], where Ω_i in Eq. (3) corresponds to the volume of a tesseroid $\left(r_1 \le \xi\left(\lambda', \varphi'\right) \le r_2;\ \varphi_1 \le \varphi' \le \varphi_2;\ \lambda_1 \le \lambda' \le \lambda_2\right)$

$$V(Q) = G \sum_i \rho_i \int_{r_1}^{r_2} \int_{\varphi_1}^{\varphi_2} \int_{\lambda_1}^{\lambda_2} \frac{\mathrm{d}\Omega}{\ell}. \tag{5}$$

The coordinates of the gravity vector with respect to the local (north/east/up) triad at the computation point Q are obtained using the partial derivatives

$$\underline{g} = \left(\frac{1}{r}\frac{\partial V}{\partial \varphi} \quad \frac{1}{r\cos\varphi}\frac{\partial V}{\partial \lambda} \quad \frac{\partial V}{\partial r}\right)^T \tag{6}$$

and the components of the symmetric Marussi tensor $\underline{\mathrm{M}} = (M_{ij})$ in the same reference frame are given by (Tscherning 1976)

$$M_{11} = \frac{1}{r^2}\left(\frac{\partial^2 V}{\partial \varphi^2} + r\frac{\partial V}{\partial r}\right), \tag{7a}$$

$$M_{12} = \frac{1}{r^2\cos\varphi}\left(\frac{\partial^2 V}{\partial \varphi \partial \lambda} + \tan\varphi\frac{\partial V}{\partial \lambda}\right) = M_{21}, \tag{7b}$$

$$M_{13} = \frac{1}{r}\left(\frac{\partial^2 V}{\partial \varphi \partial r} - \frac{1}{r}\frac{\partial V}{\partial \varphi}\right) = M_{31}, \tag{7c}$$

$$M_{22} = \frac{1}{r^2\cos^2\varphi}\left(\frac{\partial^2 V}{\partial \lambda^2} + r\cos^2\varphi\frac{\partial V}{\partial r} - \cos\varphi\sin\varphi\frac{\partial V}{\partial \varphi}\right), \tag{7d}$$

$$M_{23} = \frac{1}{r\cos\varphi}\left(\frac{\partial^2 V}{\partial r \partial \lambda} - \frac{1}{r}\frac{\partial V}{\partial \lambda}\right) = M_{32}, \tag{7e}$$

$$M_{33} = \frac{\partial^2 V}{\partial r^2}. \tag{7f}$$

The triple integrals of the potential, its first and second derivatives can be solved by purely numerical methods, e.g. the Gauss–Legendre cubature (3D) (see Appendix 1). The integral kernels of each volume integral can be found for the potential in Sect. 2.1.2 [Eq. (8)] and analogously in the Electronic Supplement A for the first and second derivatives of the potential.

Alternatively the solution of the triple, elliptic integrals can be based on different analytical and semi-analytical methods, which are described in the following Sections.

2.1.2 Taylor series expansion

One method to solve the elliptic integral is a Taylor series expansion of the integrand I of Eqs. (1) and (3)

$$I = I\left(\xi, \varphi', \lambda'\right) = \frac{\xi^2\cos\varphi'}{\sqrt{r^2 + \xi^2 - 2r\xi\cos\psi}} = \frac{\xi^2\cos\varphi'}{\ell} \tag{8}$$

and a subsequent integration. The Taylor expansion up to degree 3 can be expressed by

$$I\left(\xi, \varphi', \lambda'\right) = I\left(r_0, \varphi_0, \lambda_0\right) + \left\{\left.\frac{\partial I}{\partial \xi}\right|_0 \Delta\xi + \left.\frac{\partial I}{\partial \varphi'}\right|_0 \Delta\varphi' + \left.\frac{\partial I}{\partial \lambda'}\right|_0 \Delta\lambda'\right\}$$
$$+ \frac{1}{2}\left\{\begin{array}{l}\left.\frac{\partial^2 I}{\partial \xi^2}\right|_0 \Delta\xi^2 + 2\left.\frac{\partial^2 I}{\partial \xi \partial \varphi'}\right|_0 \Delta\xi\Delta\varphi' + 2\left.\frac{\partial^2 I}{\partial \xi \partial \lambda'}\right|_0 \Delta\xi\Delta\lambda' \\ + \left.\frac{\partial^2 I}{\partial \varphi'^2}\right|_0 \Delta\varphi'^2 + 2\left.\frac{\partial^2 I}{\partial \varphi' \partial \lambda'}\right|_0 \Delta\varphi'\Delta\lambda' + \left.\frac{\partial^2 I}{\partial \lambda'^2}\right|_0 \Delta\lambda'^2\end{array}\right\} + O\left(\Delta^3\right). \tag{9}$$

In Eq. (9) the Landau symbol $O(\Delta^3)$ indicates that terms of order three and above in $\Delta\xi$, $\Delta\varphi'$, $\Delta\lambda'$ are neglected. The Taylor point $P_0\,(r_0, \varphi_0, \lambda_0)$ is selected at the geometrical centre of the tesseroid, i.e.

$$r_0 = (r_1 + r_2)/2,\ \varphi_0 = (\varphi_1 + \varphi_2)/2, \quad \lambda_0 = (\lambda_1 + \lambda_2)/2. \tag{10}$$

Therefore, the terms of odd order and the mixed terms vanish after integration. The potential can be described as

$$V\,(Q) = G\rho \left[\begin{array}{l} I\,(r_0, \varphi_0, \lambda_0) \\ +\frac{1}{24}\left\{ \left.\frac{\partial^2 I}{\partial \xi^2}\right|_0 \Delta r^2 + \left.\frac{\partial^2 I}{\partial \varphi'^2}\right|_0 \Delta\varphi^2 + \left.\frac{\partial^2 I}{\partial \lambda'^2}\right|_0 \Delta\lambda^2 \right\} + O\left(\Delta^4\right) \end{array} \right] \Delta r\ \Delta\varphi\ \Delta\lambda, \tag{11}$$

where $\Delta r = r_2 - r_1$, $\Delta\varphi = \varphi_2 - \varphi_1$, $\Delta\lambda = \lambda_2 - \lambda_1$. The formulae of the partial derivatives are

$$I = I\,(r_0, \varphi_0, \lambda_0) = \frac{r_0^2 \cos\varphi_0}{\sqrt{r^2 + r_0^2 - 2 r r_0 \cos\psi_0}} = \frac{r_0^2 \cos\varphi_0}{\ell_0}, \tag{12a}$$

$$\left.\frac{\partial^2 I}{\partial \xi^2}\right|_0 = \frac{r^2 \cos\varphi_0}{\ell_0^5}\left\{ 2\ell_0^2 - 3 r_0^2 \sin^2\psi_0 \right\}, \tag{12b}$$

$$\begin{aligned} \left.\frac{\partial^2 I}{\partial \varphi'^2}\right|_0 = \frac{r_0^2}{\ell_0^5}\Big\{ & -\cos\varphi_0 \left(r^2 + r_0^2\right) \\ & \left(r^2 + r_0^2 - r r_0 \sin\varphi \sin\varphi_0\right) \\ & + r^2 r_0^2 \cos\varphi_0 \left(\sin^2\varphi \left(3 - \sin^2\varphi_0\right) - \cos^2\varphi \right. \\ & \left. \left(2 - \sin^2\varphi_0\right) \cos^2\Delta\lambda_0 \right), \\ & + r r_0 \cos\varphi \left(3 - \sin^2\varphi_0\right) \\ & \left(r^2 + r_0^2 - 2 r r_0 \sin\varphi \sin\varphi_0\right) \cos\Delta\lambda_0 \Big\} \end{aligned} \tag{12c}$$

$$\left.\frac{\partial^2 I}{\partial \lambda'^2}\right|_0 = -\frac{r r_0^3 \cos\varphi \cos^2\varphi_0}{\ell_0^5} \left\{ \ell_0^2 \cos\Delta\lambda_0 - 3 r r_0 \cos\varphi \cos\varphi_0 \sin^2\Delta\lambda_0 \right\}, \tag{12d}$$

$$\Delta\lambda_0 = \lambda - \lambda_0. \tag{12e}$$

To compute the components of the gravity vector and the Marussi elements, the integrands of the partial derivatives in r, ϕ, λ have to be expanded in Taylor series similarly (see Electronic Supplement A).

2.1.3 2D integrals by analytical integration over r

In this method, the Newton integral is subdivided into a 1D integral for the vertical, radial integration and a 2D spherical integral

$$V\,(Q) = G\rho \iint_\sigma \left[\int_R^{r'(\lambda',\varphi')} \frac{\xi^2}{\ell} \mathrm{d}\xi \right] \mathrm{d}\sigma, \quad \mathrm{d}\sigma = \sin\psi \mathrm{d}\psi \mathrm{d}\alpha = \cos\varphi' d\varphi' \mathrm{d}\lambda'. \tag{13}$$

The potential results, as described in e.g. Martinec (1998); Novák (2000); Novák et al. (2001); Vaníček et al. (2001); Heck (2003); Vaníček et al. (2004) in the integral

$$\begin{aligned} V\,(Q) &= \frac{G\rho}{2} \iint_\sigma \left[\xi\ell + 3 r \cos\psi \ell \right. \\ &\quad \left. + r^2 \left(3\cos^2\psi - 1\right) \ell n\left(\ell + \xi - r\cos\psi\right) \right]_R^{r'} \mathrm{d}\sigma \\ &= G\rho \iint_\sigma K_V \mathrm{d}\sigma, \end{aligned} \tag{14}$$

where

$$K_V = \frac{1}{2}\left\{ r'\bar{\ell}' - R\tilde{\ell} + 3 r \cos\psi \left(\bar{\ell}' - \tilde{\ell}\right) + r^2 \left(3\cos^2\psi - 1\right) \ell n \left| \frac{\bar{\ell}' + r' - r\cos\psi}{\tilde{\ell} + R - r\cos\psi} \right| \right\}, \tag{15a}$$

$$\bar{\ell}' = \sqrt{r^2 + r'^2 - 2 r r' \cos\psi}, \tag{15b}$$

$$\tilde{\ell} = \sqrt{r^2 + R^2 - 2 r R \cos\psi}. \tag{15c}$$

The computation of the radial derivative of the potential can be simplified with the following identity (Heck 2003)

$$\frac{\partial}{\partial r}\left(\frac{\xi^2}{\ell}\right) = \frac{2}{r}\left(\frac{\xi^2}{\ell}\right) - \frac{\partial}{\partial \xi}\left(\frac{\xi^3}{r\ell}\right). \tag{16}$$

Thus the third component of the gravity vector is

$$\begin{aligned} \frac{\partial V\,(Q)}{\partial r} &= \frac{2}{r} V\,(Q) - \frac{G\rho}{r} \iint_\sigma \left[\frac{\xi^3}{\ell} \right]_\xi \mathrm{d}\sigma \\ &= G\rho \iint_\sigma K_{V_r} \mathrm{d}\sigma, \end{aligned} \tag{17}$$

$$K_{V_r} = \frac{1}{r} \left\{ \begin{array}{l} r'\bar{\ell}' - R\tilde{\ell} + 3 r \cos\psi \left(\bar{\ell}' - \tilde{\ell}\right) \\ + r^2 \left(3\cos^2\psi - 1\right) \ell n \left| \frac{\bar{\ell}' + r' - r\cos\psi}{\tilde{\ell} + R - r\cos\psi} \right| - \frac{r'^3}{\bar{\ell}'} + \frac{R^3}{\tilde{\ell}} \end{array} \right\}. \tag{18}$$

The partial derivatives with respect to φ and λ for the computation of the gravity vector take the form

$$\frac{\partial V(Q)}{\partial \varphi} = G\rho \iint_{\sigma} K_{V_\varphi} \mathrm{d}\sigma, \tag{19}$$

$$\begin{aligned} K_{V_\varphi} = \frac{\cos\psi|_\varphi}{2} \Bigg\{ & -\frac{rr'^2}{\bar{\ell}'} + \frac{rR^2}{\tilde{\ell}} \\ & + 3r\left(\left(\bar{\ell}' - \tilde{\ell}\right) - \frac{rr'}{\bar{\ell}'}\cos\psi + \frac{rR}{\tilde{\ell}}\cos\psi\right) \\ & + 6r^2\cos\psi\,\ell n\left|\frac{\bar{\ell}' + r' - r\cos\psi}{\tilde{\ell} + R - r\cos\psi}\right| \\ & + r^3\left(3\cos^2\psi - 1\right)\left(\frac{R+\tilde{\ell}}{\tilde{\ell}\left(\tilde{\ell} + R - r\cos\psi\right)}\right. \\ & \left. - \frac{r' + \bar{\ell}'}{\bar{\ell}'\left(\bar{\ell}' + r' - r\cos\psi\right)}\right)\Bigg\}, \end{aligned} \tag{20}$$

$$\frac{\partial V(Q)}{\partial \lambda} = G\rho \iint_{\sigma} K_{V_\lambda} \mathrm{d}\sigma, \tag{21}$$

$$\begin{aligned} K_{V_\lambda} = \frac{\cos\psi|_\lambda}{2} \Bigg\{ & -\frac{rr'^2}{\bar{\ell}'} + \frac{rR^2}{\tilde{\ell}} \\ & + 3r\left(\left(\bar{\ell}' - \tilde{\ell}\right) - \frac{rr'}{\bar{\ell}'}\cos\psi + \frac{rR}{\tilde{\ell}}\cos\psi\right) \\ & + 6r^2\cos\psi\,\ell n\left|\frac{\bar{\ell}' + r' - r\cos\psi}{\tilde{\ell} + R - r\cos\psi}\right| \\ & + r^3\left(3\cos^2\psi - 1\right)\left(\frac{R+\tilde{\ell}}{\tilde{\ell}\left(\tilde{\ell} + R - r\cos\psi\right)}\right. \\ & \left. - \frac{r' + \bar{\ell}'}{\bar{\ell}'\left(\bar{\ell}' + r' - r\cos\psi\right)}\right)\Bigg\}, \end{aligned} \tag{22}$$

where

$$\begin{aligned} \cos\psi|_\varphi &= \frac{\partial\cos\psi}{\partial\varphi} = \cos\varphi\ \sin\varphi' - \sin\varphi\ \cos\varphi'\ \cos\left(\lambda - \lambda'\right), \\ \cos\psi|_\lambda &= \frac{\partial\cos\psi}{\partial\lambda} = -\cos\varphi\ \cos\varphi'\ \sin\left(\lambda - \lambda'\right). \end{aligned} \tag{23}$$

The second-order derivatives of the potential, the elements of the Marussi tensor, are attached in the Electronic Supplement B. For the computation of the second-order radial derivative, the following identity can be used (Heck and Wild 2005)

$$\begin{aligned} \frac{\partial}{\partial r^2}\left(\frac{\xi^2}{\ell}\right) = & -\frac{2}{r^2}\left(\frac{\xi^2}{\ell}\right) + \frac{\partial}{\partial r}\left(\frac{\xi^2}{\ell}\right) \\ & + \frac{\partial}{\partial \xi}\left(\frac{3\xi^3}{2r^2\ell} + \frac{\xi^3\left(r^2 - \xi^2\right)}{2r^2\ell^3}\right), \end{aligned} \tag{24}$$

resulting in

$$\begin{aligned} \frac{\partial^2 V(Q)}{\partial r^2} = & -\frac{2}{r^2}V(Q) + \frac{\partial V(Q)}{\partial r} \\ & + \frac{G\rho}{r^2}\iint_{\sigma}\left[\frac{3\xi^3}{2r^2\ell} + \frac{\xi^3\left(r^2 - \xi^2\right)}{2r^2\ell^3}\right]_\xi \mathrm{d}\sigma. \end{aligned} \tag{25}$$

Using the partition of the integration interval by means of the point $P \in S$ (see Fig. 1) into $[R, r_P]$, $[r_P, r']$, a constant term which represents the influence of a spherical shell with the constant density ρ and thickness $(r_p - R)$, and an integral term are produced. In case of the second radial derivative, the formula can be found in Heck and Wild (2005). The 2D spherical integral can be numerically evaluated, e.g. with the Gauss–Legendre cubature (2D) (see Appendix 1).

2.1.4 Approximation of the tesseroid by a prism

If a prism instead of a tesseroid is used in the ellipsoidal or in the spherical system, the effect of the potential or its first and second derivatives is obtained in the local edge system of the prism (see Sect. 2.2). Therefore, these effects have to be transformed to the local reference frame of the computation point. The best possible approximation results from two conditions:

1. Both mass elements shall have the same volume (i.e. $V_{\text{tesseroid}} = V_{\text{prism}}$) (Grüninger 1990):

$$\frac{1}{3}\left(r_2^3 - r_1^3\right)\left(\sin\varphi_2 - \sin\varphi_1\right)\left(\lambda_2 - \lambda_1\right) = \Delta x\,\Delta y\,\Delta z. \tag{26}$$

2. The height of the tesseroid is postulated to be the same as the height of the prism $\Delta r = \Delta z$.

If it is assumed that the dimensions of the tesseroid are very small ($\sin\Delta\varphi \approx \Delta\varphi$) and the distance of the tesseroid to the origin of the global (geocentric) coordinate system is very large compared to the extension of the tesseroid ($\Delta r \ll r_1$), the conversion of the tesseroid into a prism is achieved by

$$\Delta x = r_0\Delta\varphi, \quad \Delta y = r_0\cos\varphi_0\Delta\lambda, \quad \Delta z = \Delta r. \tag{27}$$

The variables are in detail

$$r_0 = (r_1 + r_2)/2, \quad \varphi_0 = (\varphi_1 + \varphi_2)/2, \quad \Delta\lambda = \lambda_2 - \lambda_1. \tag{28}$$

The transformation of the local edge system of the prism into the system of the computation point is given with the aid of a conventional, global geodetic coordinate system, because it is assumed that the spatial Cartesian or geodetic coordinates of the computation point Q and the point P' in the centre of the top surface are known (see Fig. 3). The effect of the deviations of the vertical is neglected in the following.

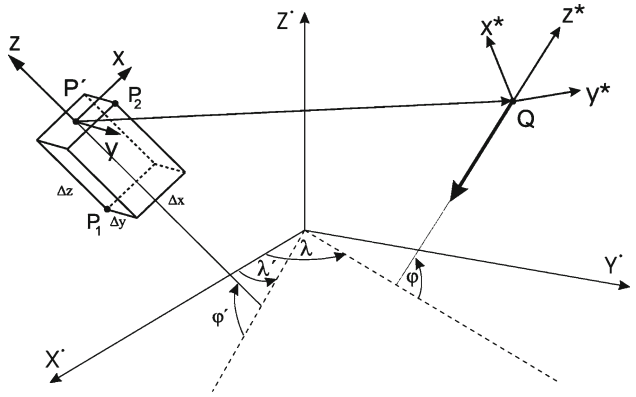

Fig. 3 Transformation of the local edge system of the prism in the reference system of the computation point

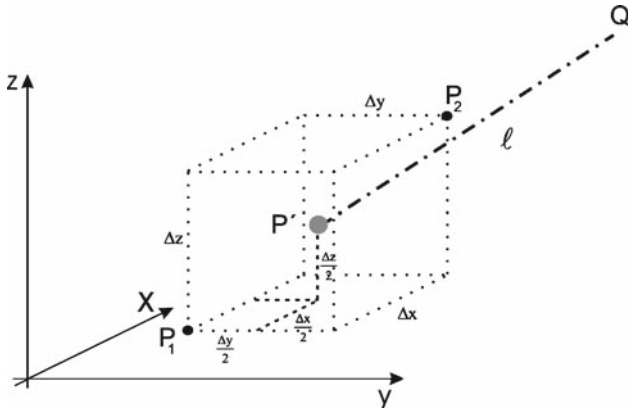

Fig. 4 Prism and point mass in the local coordinate system

The equation of the transformation for the gravity vector is (Grüninger 1990; Kuhn 2000)

$$\underline{g}^* = \underbrace{\underline{S}_x \underline{R}_y \left(\frac{\pi}{2} - \varphi\right) \underline{R}_z (\lambda) \left(\underline{S}_x \underline{R}_y \left(\frac{\pi}{2} - \varphi'\right) \underline{R}_z (\lambda')\right)^T}_{\underline{R}} \underline{g}, \tag{29}$$

where $\underline{R}_y$ and $\underline{R}_z$ denote rotation matrices for rotation about the y and z axes, respectively, while $\underline{S}_x$ indicates a mirroring of the x axis. The complete transformation matrix $\underline{\mathrm{R}}$ is given by

$$\underline{R} = \begin{pmatrix} c_1 \sin\varphi \sin\varphi' + \cos\varphi \cos\varphi' & c_2 \sin\varphi & -c_1 \sin\varphi \cos\varphi' + \cos\varphi \sin\varphi' \\ -c_2 \sin\varphi' & c_1 & c_2 \cos\varphi' \\ -c_1 \cos\varphi \sin\varphi' + \sin\varphi \cos\varphi' & -c_2 \cos\varphi & c_1 \cos\varphi \cos\varphi' + \sin\varphi \sin\varphi' \end{pmatrix}, \tag{30}$$

where

$$c_1 = \cos\lambda \cos\lambda' + \sin\lambda \sin\lambda' = \cos\left(\lambda - \lambda'\right), \tag{31a}$$

$$c_2 = \sin\lambda \cos\lambda' - \cos\lambda \sin\lambda' = \sin\left(\lambda - \lambda'\right). \tag{31b}$$

The Marussi tensor in the local system of the computation point is obtained from

$$\underline{M}^* = \underline{R} \underline{M} \underline{R}^T, \tag{32}$$

where $\underline{M}$ denotes the representation of the Marussi tensor in the edge system of the prism.

2.2 Prism

In the immediate vicinity of the computation point, where the digital elevation model (DEM) normally is provided in a Cartesian grid (e.g. Gauss–Krüger or UTM coordinates), the terrain can be subdivided into prisms. A local coordinate system is defined for every prism, which is aligned along the edges of the prism. The direction of the z-axis is in radial direction, in opposite to the local plumbline; the x- and y-axes are situated in the local tangential plane and are directed to North and East (see Fig. 4).

The potential of a prism in an arbitrary computation point Q generally results from the Newton integral [Eq. (1)] in Cartesian coordinates where

$$\mathrm{d}V = dx'\,\mathrm{d}y'\,\mathrm{d}z', \quad \ell = \sqrt{(x-x')^2 + (y-y')^2 + (z-z')^2} = \sqrt{\bar{x}^2 + \bar{y}^2 + \bar{z}^2}, \quad \rho\left(x', y', z'\right). \tag{33}$$

With a homogeneous mass distribution, the potential of a prism is (Mader 1951)

$$V(Q) = G\rho \left[\begin{array}{l} -\bar{y}\bar{z} \log\left(\bar{x} + \ell\right) - \bar{x}\bar{y} \log\left(\bar{z} + \ell\right) - \bar{x}\bar{z} \log\left(\bar{y} + \ell\right) \\ \\ \quad + \frac{\bar{x}^2}{2} \arctan \frac{\bar{y}\bar{z}}{\bar{x}\ell} + \frac{\bar{y}^2}{2} \arctan \frac{\bar{x}\bar{z}}{\bar{y}\ell} + \frac{\bar{z}^2}{2} \arctan \frac{\bar{y}\bar{x}}{\bar{z}\ell} \end{array} \right]_{x_1, y_1, z_1}^{x_2, y_2, z_2}. \tag{34}$$

The components of the gravity vector and the elements of the Marussi tensor at the computation point Q are listed in Mader (1951) and in the Electronic Supplement C. The equations of the potential and its first and second order derivates show singularities, depending on the position of the computation point, e.g., when the computation point coincides with an edge of the prism, i.e. $x = x_1$, $y = y_1$, or $z = z_1$. In this case the arctan-function is not defined; in Nagy et al. (2000, 2002) it is shown that these terms can be set equal to zero. In

Tsoulis (1999), all the singularities are listed which can occur in computing the potential, the first or the second derivatives of a prism in Cartesian coordinates.

In the case of a spherical grid, a transformation of the gravity vector and the Marussi tensor from the edge system of the prism into the local system of the computation point Q is necessary, see Eqs. (29)–(32). This remark applies also for the point mass (see Sect. 2.3), the mass layer (see Sect. 2.4) and the mass line (see Sect. 2.5).

2.3 Point mass

The effect of the distant masses can be approximated by point masses, each located at the geometrical centre $P' = P_0$ of the tesseroid; the mass at P_0 is assumed to be equal to the mass of the tesseroid. It can easily be proved that the effect of a point mass is equal to the zero-order term of the Taylor expansion described in Sect. 2.1.2. For the potential, Eq. (11) leads to

$$V = G\rho \left[\frac{\xi^2 \cos\varphi'}{\sqrt{r^2 + \xi^2 - 2r\xi\cos\psi}} \right]\Bigg|_0 \Delta r\ \Delta\varphi\ \Delta\lambda. \tag{35}$$

The effect of a point mass can also be obtained when the mass of a prism (see Sect. 2.2) $M = \rho \cdot \Delta x \cdot \Delta y \cdot \Delta z$ is concentrated at the midpoint (see Fig. 4)

$$V(Q) = \frac{GM}{\ell} = G\rho \frac{\Delta x \Delta y \Delta z}{\ell}. \tag{36}$$

The formulae of the gravitational attraction can be found in Grüninger (1990) and in the Electronic Supplement D. The elements of the Marussi tensor are

$$M_{xx}(Q) = \frac{\partial^2 V(Q)}{\partial x^2} = G\rho\Delta x\Delta y\Delta z \left[-\frac{1}{\ell^3} + \frac{3\bar{x}^2}{\ell^5} \right], \tag{37a}$$

$$M_{xy}(Q) = \frac{\partial^2 V(Q)}{\partial x \partial y} = G\rho\Delta x\Delta y\Delta z \left[\frac{3\bar{x}\bar{y}}{\ell^5} \right] = M_{yx}(Q), \tag{37b}$$

$$M_{xz}(Q) = \frac{\partial^2 V(Q)}{\partial x \partial z} = G\rho\Delta x\Delta y\Delta z \left[\frac{3\bar{x}\bar{z}}{\ell^5} \right] = M_{zx}(Q), \tag{37c}$$

$$M_{yy}(Q) = \frac{\partial^2 V(Q)}{\partial y^2} = G\rho\Delta x\Delta y\Delta z \left[-\frac{1}{\ell^3} + \frac{3\bar{y}^2}{\ell^5} \right], \tag{37d}$$

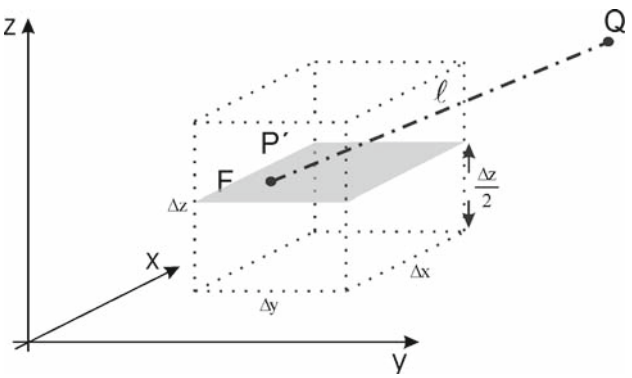

Fig. 5 Planar mass layer as an approximation of a prism

$$M_{yz}(Q) = \frac{\partial^2 V(Q)}{\partial y \partial z} = G\rho\Delta x\Delta y\Delta z \left[\frac{3\bar{y}\bar{z}}{\ell^5} \right] = M_{zy}(Q), \tag{37e}$$

$$M_{zz}(Q) = \frac{\partial^2 V(Q)}{\partial z^2} = G\rho\Delta x\Delta y\Delta z \left[-\frac{1}{\ell^3} + \frac{3\bar{z}^2}{\ell^5} \right]. \tag{37f}$$

2.4 Mass layer

The effect of a prism can be replaced by a mass layer at half height $\Delta z/2$, if the side lengths Δx, Δy are large compared to the height Δz of the prism (see Fig. 5). The mass of the prism is condensed on a planar, horizontal layer with a surface density $\rho_F = \rho \cdot \Delta z$.

The potential is

$$V(Q) = G \iint_F \frac{\rho_F}{\ell}\, dF = G \iint_F \frac{\rho}{\ell} \Delta z \cdot dx' dy', \tag{38}$$

explicitly

$$V(Q) = G\rho\Delta z \left[\bar{x}\log(\bar{y} + \ell) + \bar{y}\log(\bar{x} + \ell) - \bar{z}\arctan\frac{\bar{x}\bar{y}}{\bar{z}\ell} \right]\Bigg|_{x_1,y_1}^{x_2,y_2}, \tag{39a}$$

$$\bar{x} = x - x',\ \bar{y} = y - y',\ \bar{z} = z - z',\ z' = (z_1 + z_2)/2,\ \ell = \sqrt{\bar{x}^2 + \bar{y}^2 + \bar{z}^2}. \tag{39b}$$

The gravity effect of a mass layer is listed in Grüninger (1990) and in the Electronic Supplement E and the second

derivatives of the potential are obtained via the formulae

$$M_{xx}(Q) = \frac{\partial^2 V(Q)}{\partial x^2}$$
$$= G \iint_F \rho \left[-\frac{1}{\ell^3} + \frac{3\bar{x}^2}{\ell^5} \right] \Delta z \, \mathrm{d}x' \, \mathrm{d}y'$$
$$= -G\rho\Delta z \left[\frac{\bar{x}\bar{y}}{\left(\bar{x}^2 + \bar{z}^2\right)\ell} \right]\Bigg|_{x_1,y_1}^{x_2,y_2}, \tag{40a}$$

$$M_{xy}(Q) = \frac{\partial^2 V(Q)}{\partial x \partial y}$$
$$= G \iint_F \rho \left[\frac{3\bar{x}\bar{y}}{\ell^3} \right] \Delta z \, \mathrm{d}x' \, \mathrm{d}y'$$
$$= G\rho\Delta z \, \frac{1}{\ell}\Bigg|_{x_1,y_1}^{x_2,y_2}$$
$$= M_{yx}(Q), \tag{40b}$$

$$M_{xz}(Q) = \frac{\partial^2 V(Q)}{\partial x \partial z}$$
$$= G \iint_F \rho \left[\frac{3\bar{x}\bar{z}}{\ell^3} \right] \Delta z \, \mathrm{d}x' \, \mathrm{d}y'$$
$$= -G\rho\Delta z\bar{z} \, \frac{\bar{y}}{\left(\bar{x}^2 + \bar{z}^2\right)\ell}\Bigg|_{x_1,y_1}^{x_2,y_2}$$
$$= M_{zx}(Q), \tag{40c}$$

$$M_{yy}(Q) = \frac{\partial^2 V(Q)}{\partial y^2}$$
$$= G \iint_F \rho \left[-\frac{1}{\ell^3} + \frac{3\bar{y}^2}{\ell^5} \right] \Delta z \, \mathrm{d}x' \, \mathrm{d}y'$$
$$= -G\rho\Delta z \, \frac{\bar{x}\bar{y}}{\left(\bar{y}^2 + \bar{z}^2\right)\ell}\Bigg|_{x_1,y_1}^{x_2,y_2}, \tag{40d}$$

$$M_{yz}(Q) = \frac{\partial^2 V(Q)}{\partial y \partial z} G \iint_F \rho \left[\frac{3\bar{y}\bar{z}}{\ell^3} \right] \Delta z \, \mathrm{d}x' \, \mathrm{d}y'$$
$$= -G\rho\Delta z\bar{z} \, \frac{\bar{x}}{\left(\bar{y}^2 + \bar{z}^2\right)\ell}\Bigg|_{x_1,y_1}^{x_2,y_2}$$
$$= M_{zy}(Q), \tag{40e}$$

$$M_{zz}(Q) = \frac{\partial^2 V(Q)}{\partial z^2}$$
$$= G \iint_F \rho \left[-\frac{1}{\ell^3} + \frac{3\bar{z}^2}{\ell^5} \right] \Delta z \, \mathrm{d}x' \, \mathrm{d}y'$$
$$= G\rho\Delta z \, \frac{\bar{y}\bar{x}\left(\bar{x}^2 + \bar{y}^2 + 2\bar{z}^2\right)}{\ell\left(\bar{x}^2 + \bar{z}^2\right)\left(\bar{y}^2 + \bar{z}^2\right)}\Bigg|_{x_1,y_1}^{x_2,y_2}. \tag{40f}$$

In case of a mass layer, a singularity is produced if the z-component of the computation point equals the z'-component of the integration point, i.e. $\bar{z} = 0$. In case of gradiometric measurements at satellite height, as in the forthcoming GOCE mission, this singularity is irrelevant.

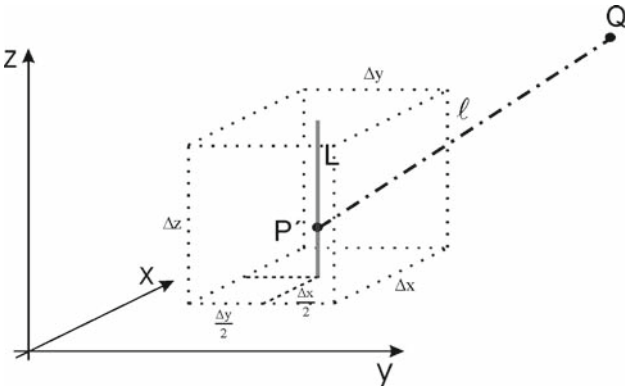

Fig. 6 Vertical mass line as an approximation of a prism

2.5 Vertical mass line

If the height Δz of a prism is large in comparison with its side lengths, a vertical mass line is suited for the approximation. Here the mass is condensed along a vertical line in the middle of the prism $(\Delta x/2, \Delta y/2)$; the line density is $\rho_L = \rho\Delta x\Delta y$ (see Fig. 6).

The potential of a mass line is computed with the Newton integral in Cartesian coordinates [Eq. (1)]

$$V(Q) = G \int_L \frac{\rho_L}{\ell} \, dL = G \int_L \frac{\rho}{\ell} \Delta x \Delta y dL. \tag{41}$$

In Cartesian coordinates, the potential is expressed by

$$V(Q) = G \int_z \frac{\rho}{\ell} \Delta x \Delta y \mathrm{d}z$$
$$= G\rho\Delta x\Delta y \, \log\left(\bar{z} + \ell\right)\Big|_{z_1}^{z_2}, \tag{42}$$

$$\bar{x} = x - x', \quad \bar{y} = y - y', \quad \bar{z} = z - z', \quad x' = (x_1 + x_2)/2,$$
$$y' = (y_1 + y_2)/2, \quad \ell = \sqrt{\bar{x}^2 + \bar{y}^2 + \bar{z}^2}. \tag{43}$$

In Grüninger (1990) and the Electronic Supplement F, the gravity vector is illustrated. The Marussi tensor can be expressed by

$$M_{xx}(Q) = \frac{\partial^2 V(Q)}{\partial x^2}$$
$$= G \int_z \rho \left[-\frac{1}{\ell^3} + \frac{3\bar{x}^2}{\ell^5} \right] \Delta x \Delta y \mathrm{d}z'$$
$$= G\rho\Delta x\Delta y$$
$$\left[\frac{\bar{z}\left(2\bar{x}^4 + \bar{x}^2\bar{y}^2 + \bar{z}^2\bar{x}^2 - \bar{y}^4 - \bar{y}^2\bar{z}^2\right)}{\left(\bar{x}^2 + \bar{y}^2\right)^2 \ell^3} \right]\Bigg|_{z_1}^{z_2}, \tag{44a}$$

$$M_{xy}(Q) = \frac{\partial^2 V(Q)}{\partial x \partial y} = G \int_z \rho \left[\frac{3\bar{x}\bar{y}}{\ell^5} \right] \Delta x \Delta y \mathrm{d}z'$$

$$= G\rho \Delta x \Delta y \left[\frac{\bar{x}\bar{y}\bar{z}\left(3\bar{x}^2 + 3\bar{y}^2 + 2\bar{z}^2\right)}{\left(\bar{x}^2 + \bar{y}^2\right)^2 \ell^3} \right]\Bigg|_{z_1}^{z_2}$$

$$= M_{yx}(Q), \tag{44b}$$

$$M_{xz}(Q) = \frac{\partial^2 V(Q)}{\partial x \partial z} = G \int_z \rho \left[\frac{3\bar{x}\bar{z}}{\ell^5} \right] \Delta x \Delta y \mathrm{d}z'$$

$$= G\rho \Delta x \Delta y \left[\frac{-\bar{x}}{\ell^3} \right]\Bigg|_{z_1}^{z_2}$$

$$= M_{zx}(Q), \tag{44c}$$

$$M_{yy}(Q) = \frac{\partial^2 V(Q)}{\partial y^2}$$

$$= G \int_z \rho \left[-\frac{1}{\ell^3} + \frac{3\bar{y}^2}{\ell^5} \right] \Delta x \Delta y \mathrm{d}z'$$

$$= G\rho \Delta x \Delta y \left[\frac{-\bar{z}\left(\bar{x}^4 - \bar{x}^2\bar{y}^2 + \bar{z}^2\bar{x}^2 - 2\bar{y}^4 - \bar{y}^2\bar{z}^2\right)}{\left(\bar{x}^2 + \bar{y}^2\right)^2 \ell^3} \right]\Bigg|_{z_1}^{z_2}, \tag{44d}$$

$$M_{yz}(Q) = \frac{\partial^2 V(Q)}{\partial y \partial z}$$

$$= G \int_z \rho \left[\frac{3\bar{y}\bar{z}}{\ell^5} \right] \Delta x \Delta y \mathrm{d}z'$$

$$= G\rho \Delta x \Delta y \left[\frac{-\bar{y}}{\ell^3} \right]\Bigg|_{z_1}^{z_2}$$

$$= M_{zy}(Q), \tag{44e}$$

$$M_{zz}(Q) = \frac{\partial^2 V(Q)}{\partial z^2} = G \int_z \rho \left[-\frac{1}{\ell^3} + \frac{3\bar{z}^2}{\ell^5} \right] \Delta x \Delta y \mathrm{d}z' = -G\rho \Delta x \Delta y \left[\frac{\bar{z}}{\ell^3} \right]\Bigg|_{z_1}^{z_2}. \tag{44f}$$

Singularities in case of the mass line exist for $\bar{x} = \bar{y} = 0$ and can occur also in satellite gradiometry. In this case, the mass elements which are situated in the immediate vicinity of the computation point are affected and therefore handled by the prism approximation (see Sect. 2.2).

3 Numerical tests

3.1 Comparison of the different computation methods: synthetic example

The presented formulae for the different mass elements and computation methods for the potential, the gravity vector and the Marussi tensor are evaluated for the case of the second-order derivatives for a spherical cap around the computation point. In particular, the elements of the Laplace equation M_{xx}, M_{yy} and M_{zz} are calculated for a synthetic topography of constant height (1,000 m), when the dimension of the tesseroids is $5' \times 5'$ and the computation point Q is situated on the polar axis. The height of the point Q is 260 km, approximately equivalent to the flight height of the forthcoming GOCE (Gravity and Steady-State Ocean Circulation Experiment) mission. The spherical cap of constant topographical height presents in some way a worst case scenario which can be used to evaluate the precision of the integration procedure and the respective computation times.

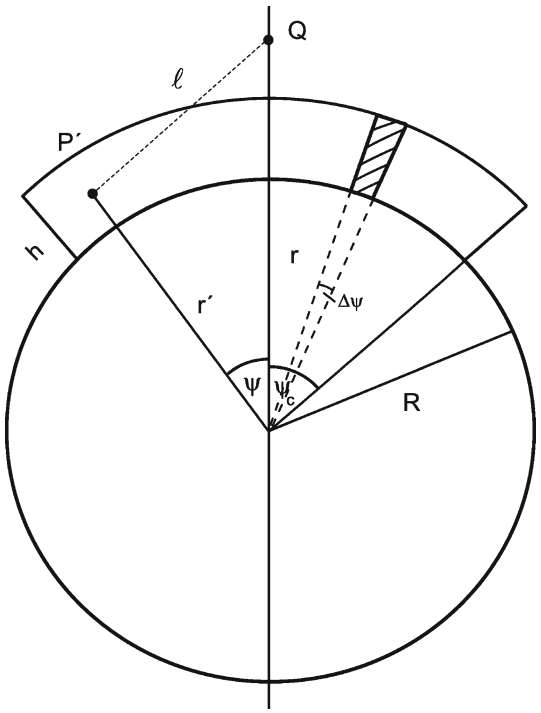

Fig. 7 Test configuration: spherical cap, computation point on the symmetry (polar) axis

For the polar position of the computation point, an exact analytical solution for a tesseroid exists (see Fig. 7). Therefore the results of the modelling by different mass elements and methods for each ring zone ($\Delta\psi = 5'$) are compared with those of the exact, closed formula for the spherical cap (Kühtreiber et al. 1989; Heck and Seitz 2007). The effect of any ring zone can be derived from the difference of the effects of two subsequent spherical caps with spherical radii $\psi_{c,i}, \psi_{c,i+1}$, where $\Delta\psi = \psi_{c,i+1} - \psi_{c,i} = 5'$. Each ring zone is divided in to tesseroids of the base area $5' \times 5'$ and of the height $h = 1{,}000$ m. The components of the Marussi tensor are achieved by differentiating the potential with respect to r, φ, λ.

In this special symmetric test example the Marussi tensor has a diagonal form, specifically $M_{xx} = M_{yy} = -1/2 M_{zz}$. This can be proved by a principle axis transformation for a

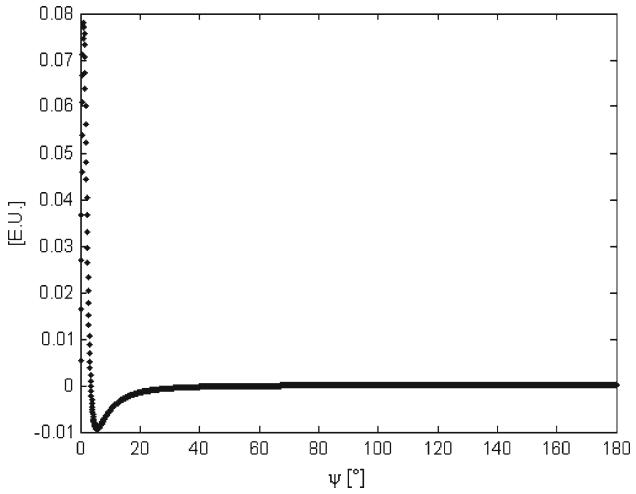

Fig. 8 Effect of a spherical cap zone (latitude band, width $\Delta\psi = 5'$) on M_{zz}; density $\rho = 2{,}670\,\mathrm{kg}\cdot\mathrm{m}^{-3}$; height 1,000 m

symmetric tensor. In Fig. 8, the effect of spherical cap zones, i.e. ring zones around the computation point with $\Delta\psi = 5'$, are presented for subsequent radii up to $\psi = 180°$, using parameters $G = 6.673\cdot10^{-11}\,\mathrm{m}^3\cdot\mathrm{kg}^{-1}\cdot\mathrm{s}^{-2}$, $\rho = 2{,}670\,\mathrm{kg}\cdot\mathrm{m}^{-3}$, $R = 6{,}378137$ m (i.e. Brillouin sphere: $R = a$), $h = 1{,}000$ m. The maximum effect of a cap zone exists for a spherical radius of about 1.6°.

Table 1 lists the maximum difference between the exact value of the spherical cap zone and the modelling by different mass elements (tesseroid, point mass, prism, mass line and mass layer) and computation methods per concentric ring zone. Furthermore, it presents the cumulated error of M_{zz} when the integration is extended over the total spherical cap $\psi_c = 10°$, the near zone of the computation point (see numerical examples in Heck and Seitz 2007). Figure 9 shows the approximation error per ring zone and Fig. 10 the total error in the Marussi element M_{zz} by integration up to $\psi_c = 10°$. Table 1, Figs. 9 and 10 illustrate that the evaluation of ring zones using tesseroids computed by a Taylor series expansion best approximates the exact value of a spherical cap. It is evident from Figs. 9 and 10 that the point mass and mass line approximations behave in practically the same way, similarly the mass layer and prism methods. These properties can easily be explained by considering the horizontal and vertical extension of the mass elements with respect to their distance from the computation point Q. The total error of the point mass and mass line approximations for the spherical cap is about $4.6\cdot10^{-4}$ E.U., and better by a factor of 1.5 than the mass layer and prism methods. The total error of a tesseroid computed by a Taylor series expansion is three orders of magnitude smaller than the other mass elements.

It is evident in Table 1 that all the mass elements which have to be transformed from a tesseroid to a prism, produce larger deviations in regard to the analytical solution.

Table 1 Maximum error in M_{zz} for a concentric ring zone ($\Delta\psi = 5'$) /total error for a spherical cap ($\psi_c = 10°$) concerning different mass elements and tesseroid height 1,000 m (absolute value of M_{zz}: 0.6228 E.U.)

Mass element	Maximum error for a 5′ ring zone in M_{zz} (E.U.)	Total error for a spherical cap in M_{zz} (E.U.)
Point mass	5.06505×10^{-5}	-4.56971×10^{-4}
Mass line	5.09955×10^{-5}	-4.56912×10^{-4}
Mass layer	4.52783×10^{-5}	-9.22607×10^{-4}
Prism	4.55422×10^{-5}	-9.22550×10^{-4}
Tesseroid-Taylor	2.28325×10^{-8}	1.31502×10^{-7}

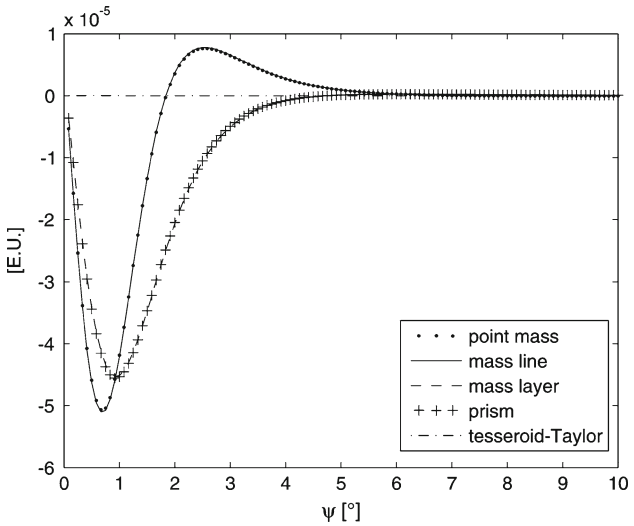

Fig. 9 Approximation error of M_{zz} (E.U.) for a concentric ring zone $\Delta\psi = 5'$ and tesseroid height 1,000 m concerning different mass elements

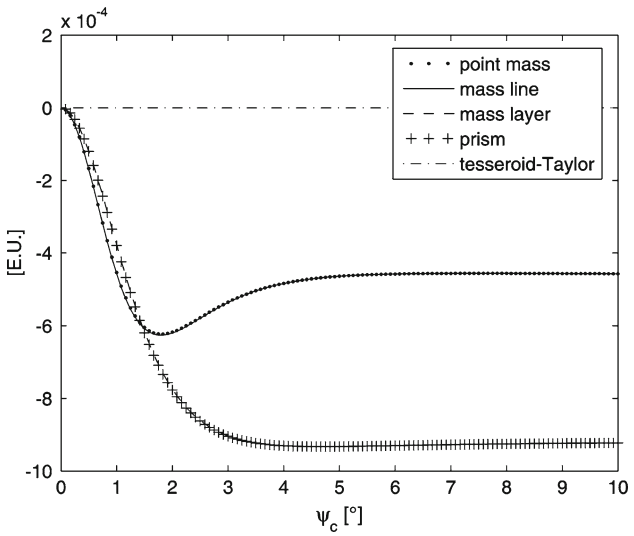

Fig. 10 Total error of M_{zz} (E.U.) for a spherical cap (spherical radius ψ_c, height 1,000 m) concerning different mass elements

Table 2 Maximum error in M_{zz} for a concentric ring zone ($\Delta\psi = 5'$) /total error for a spherical cap ($\psi_c = 10°$) concerning the radial analytical integration + Gauss–Legendre cubature (2D) for $0 \le n = m \le 5$ and tesseroid height 1,000 m

$n = m$	Maximum error for a 5′ ring zone in M_{zz} (E.U.)	Total error for a spherical cap in M_{zz} (E.U.)
0	5.10129×10^{-5}	-4.56932×10^{-4}
1	1.04617×10^{-8}	5.59172×10^{-8}
2	5.57690×10^{-12}	-8.47530×10^{-10}
3	5.57690×10^{-12}	-8.46780×10^{-10}
4	5.57680×10^{-12}	-8.46570×10^{-10}
5	5.57670×10^{-12}	-8.46570×10^{-10}

Table 3 Maximum error in M_{zz} for a concentric ring zone ($\Delta\psi = 5'$) /total error for a spherical cap ($\psi_c = 10°$) concerning the Gauss–Legendre cubature (3D) for $0 \le n = m = p \le 2$ and tesseroid height 1,000 m

$n = m = p$	Maximum error for a 5′ ring zone in M_{zz} (E.U.)	Total error for a spherical cap in M_{zz} (E.U.)
0	5.06505×10^{-5}	-4.59729×10^{-5}
1	1.04628×10^{-8}	6.00153×10^{-8}
2	5.57680×10^{-12}	5.06000×10^{-12}

A potential explanation for the errors in the case of point mass approximations etc. is the convergence of the coordinate lines at the computation point: In the direct surrounding of the computation point triangular elements are replaced by rectangles.

Tables 2 and 3 and Figs. 11, 12 and 13 make it clear that the tesseroid, modelled by an analytical, vertical integration and Gauss–Legendre cubature (2D) or Gauss–Legendre cubature (3D), depending on the values n, m and p of the quadrature formula, provides very good results. In case of the M_{zz}-component, the computation time is approximately a tenth of the computation time for a prism (Fig. 14). The point mass, as the zero-order term of the Taylor series expansion, needs less computer time than the point mass, which results from the approximation of a tesseroid by a prism because in the latter case a transformation from the local system of the prism into the system of the computation point is required. In Figs. 14, 15 and 16, the computation time for each mass element is normalized with respect to the computation time for a prism which has been set equal to 1.

Table 2 lists the maximum difference between the exact value of the spherical cap zone and the modelling by tesseroids using the vertical, analytical integration and Gauss–Legendre cubature (2D) for $0 \le n = m \le 5$. Figure 11 illustrates the approximation error of the Marussi element M_{zz} induced by spherical cap zones $\Delta\psi = 5'$. In this computation, the first parallel 0′–5′ is excluded because of the

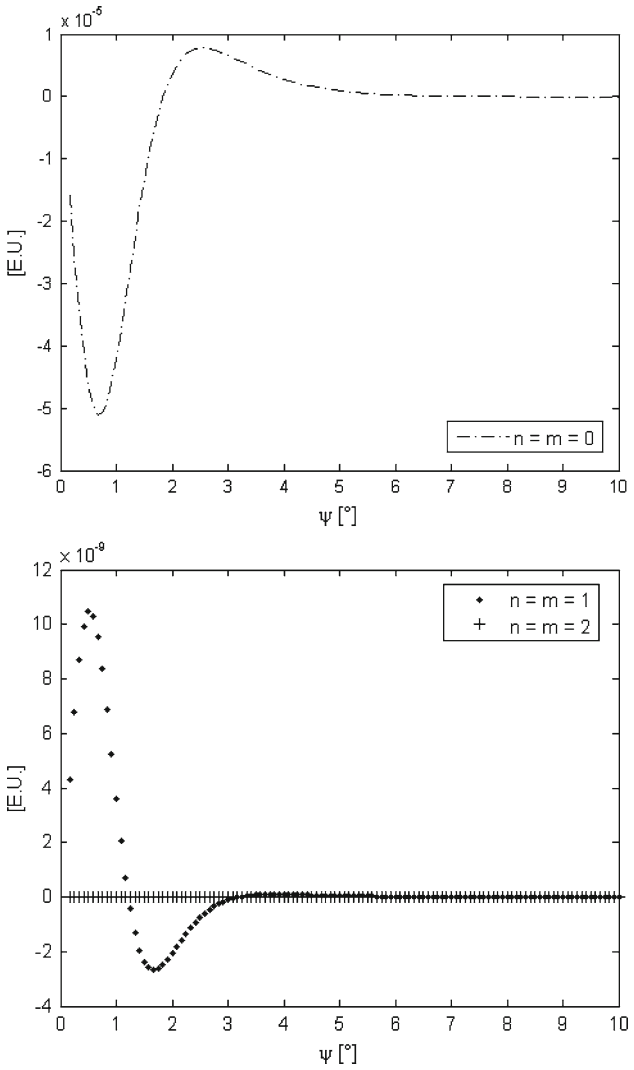

Fig. 11 Approximation error of M_{zz} (E.U.) for a concentric ring zone $\Delta\psi = 5'$ and tesseroid height 1,000 m concerning the vertical, analytical integration and Gauss–Legendre cubature (2D) for $0 \le n = m \le 2$

singularity of the integral kernel. In general, the "singularities" around the computation point can be modelled by prisms. It is shown that $n = m = 0$ deviates most from the exact solution; for $2 \le n = m \le 5$ the deviation is practically equal and very small (10^{-12} E.U.). In comparison the accuracy of the GOCE mission is about 1–2 mE.U.. Figure 12 shows that the integrated error for the total spherical cap of cap size ψ_c in case of $n = m = 0$ has the same order of magnitude as the total error of the mass elements derived from the prism. For $n = m = 1$ up to higher values, the total error is better by a factor 0.5 ($n = m = 1$) and $2 \cdot 10^{-2}$($2 \le n = m \le 5$) than the modelling by a Taylor series expansion. The cumulated error for the integration over a spherical cap of radius $\psi_c = 10°$, presented in Table 2, provides analogous results. Therefore $n = m = 1$ yields an acceptable result in view of the increasing number

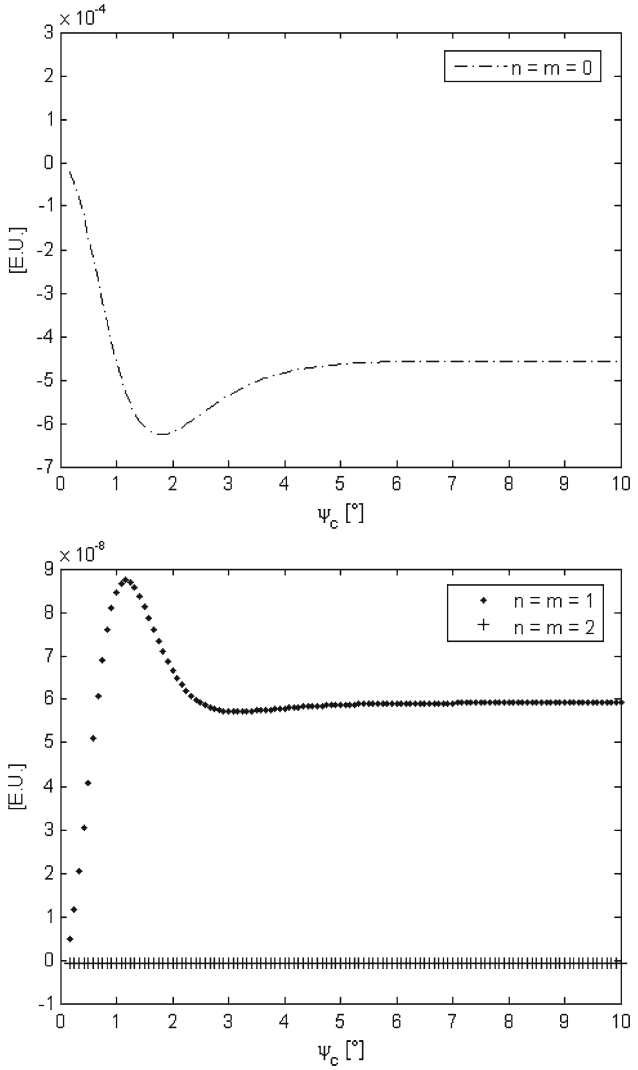

Fig. 12 Total error of M_{zz} (E.U.) for a a spherical cap (spherical radius ψ_c, height 1,000 m) concerning the vertical, analytical integration and Gauss–Legendre cubature (2D) for $0 \leq n = m \leq 2$

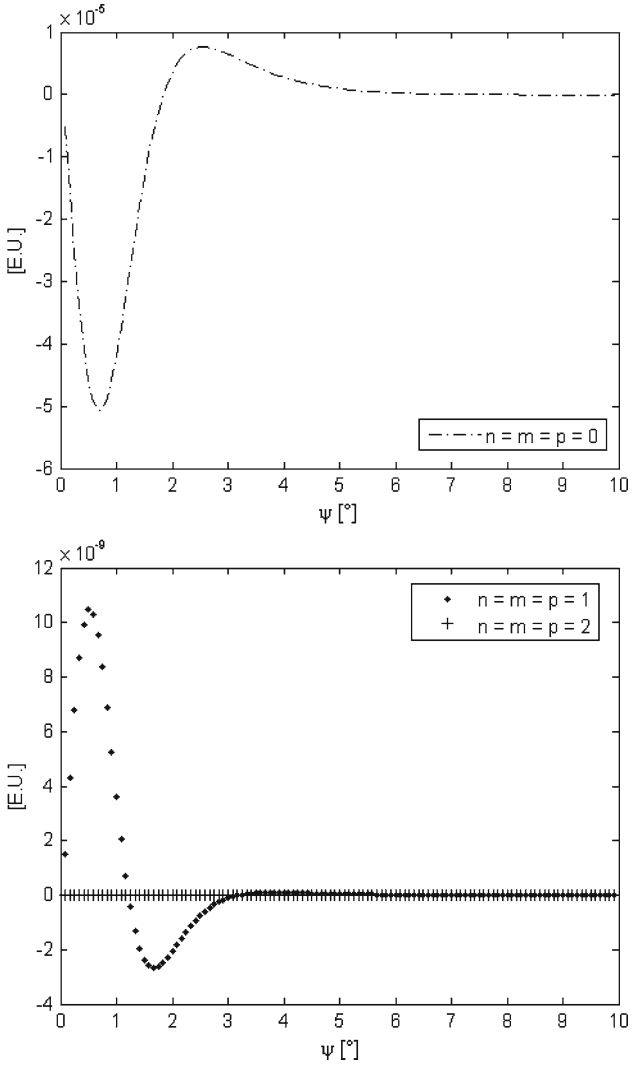

Fig. 13 Approximation error of M_{zz} (E.U.) for a concentric ring zone $\Delta\psi = 5'$ and tesseroid height 1,000 m concerning the Gauss–Legendre cubature (3D) for $0 \leq n = m = p \leq 2$

of function evaluations and the computation time (see Fig. 15) with increasing values of n and m.

The maximum difference between the exact value of the spherical cap zone and the numerical modelling by tesseroids using the Gauss–Legendre cubature (3D) for $0 \leq n = m = p \leq 2$ is specified in Table 3. Figure 13 shows the approximation error of the Marussi element M_{zz} induced by spherical cap zones $\Delta\psi = 5'$. The total error in Table 3 equals the error of the modelling by tesseroids using analytical integration and Gauss–Legendre cubature (2D) (see Table 2; Fig. 12). Analogously to the 2D-case, $n = m = p = 2$ yields the most exact result (10^{-12} E.U.) of the values presented in Table 2. Regarding the increasing number of function evaluations and the computation speed, which is slower than in the 2D-case because of the much simpler integral kernel (see Fig. 16), $n = m = p = 1$ provides a good approximation. In Wild-Pfeiffer (2007) it is argued that a higher number of function evaluations in the vertical dimension ($n = m = 1$, $p = 2$) may be an alternative to get a more exact result in an acceptable computation time.

3.2 Topographical effects in satellite gravity gradiometry

The effect of the topographic mass model at height of the GOCE satellite has been calculated via tesseroid modelling using Gauss–Legendre cubature (3D) for $n = m = p = 1$ (8 nodes per element). This numerical modelling is favoured because it is sufficient in a low computation time (see Sect. 3.1).

The numerical parameters used in the computation are $R = 6{,}378{,}137$ m and $G = 6.673 \cdot 10^{-11}\,\mathrm{m^3\,kg^{-1}\,s^{-2}}$. The satellite height is 260 km. The digital terrain model JGP95E

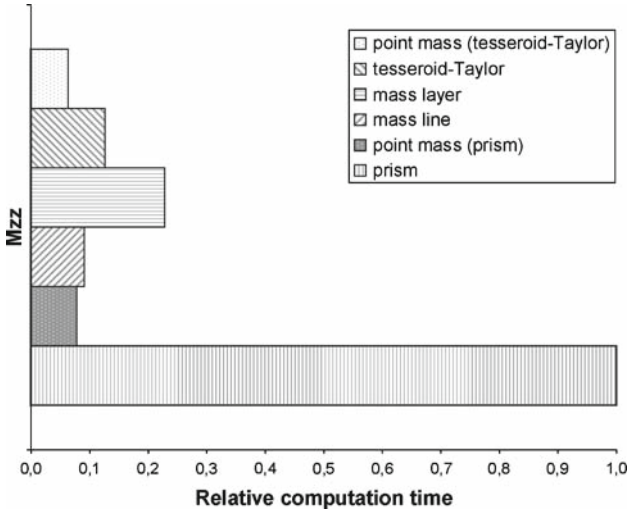

Fig. 14 Comparison of different mass elements concerning the computation time

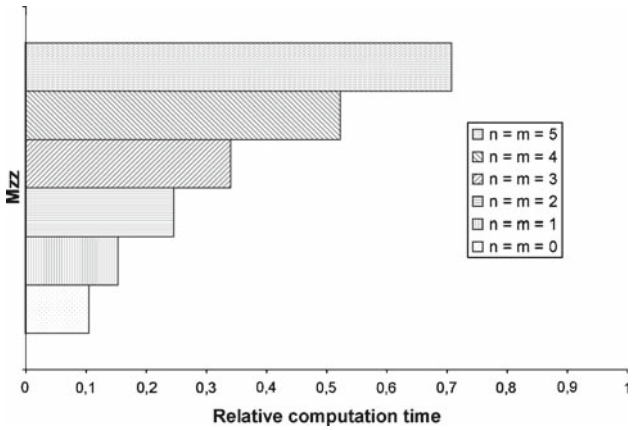

Fig. 15 Comparison of the modelling by tesseroids (analytical integration in r and Gauss–Legendre cubature (2D)) for $0 \leq n = m \leq 5$ concerning the computation time

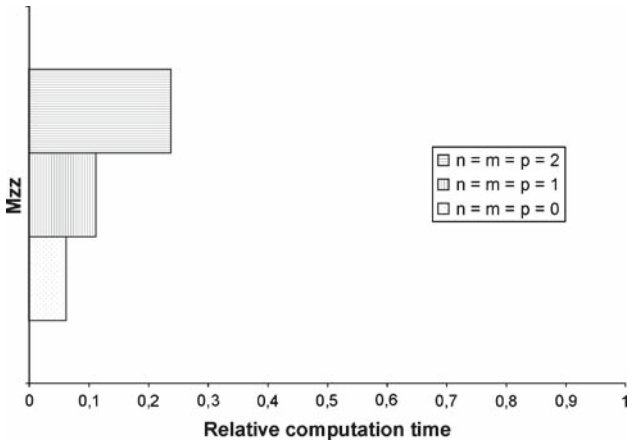

Fig. 16 Comparison of the modelling by tesseroids (Gauss–Legendre cubature (3D)) for $0 \leq n = m = p \leq 2$ concerning the computation time

"rock-equivalent" has a resolution $0.5° \times 0.5°$. The density of the crust is $\rho_0 = 2670\,\mathrm{kg} \cdot \mathrm{m}^{-3}$. Figure 17 displays the Marussi tensor of the topographic effect with the order of magnitude of about ±8E.U.

The isostatic effect has the same order of magnitude as the topographic effect, but the combined effect varies for the different isostatic and condensation models (Wild and Heck 2004, 2005; Wild-Pfeiffer and Heck 2006). In case of the Airy-Heiskanen model the combined effect is about ±0.8 E.U.

If GOCE data are available quantitative statements with regard to the choice of the isostatic model, the order of magnitude of the topographic-isostatic effect and the smoothing in terms of the downward continuation can be made. Furthermore it is evident that the topographic-isostatic signals of specific geological structures can effectively be utilized for the external calibration of the GOCE gravity gradiometer (Koop et al. 2001; Bouman and Koop 2003).

4 Conclusions

Some alternative mass elements and computation methods for the description of the gravitational effects of topographic and isostatic masses in satellite gravity gradiometry are derived and checked. The numerical results demonstrate that the tesseroid modelled by different methods provides the most accurate approach compared to the exact solution of a spherical shell. The modelling by an analytical integration in r and Gauss–Legendre cubature (2D) or a Gauss–Legendre cubature (3D) is practically equivalent for $n = m = p = 2$. The modelling by a Taylor series expansion is worse by a factor of 2. The computation time for these three cases is nearly equivalent. The 2D-cubature method is slightly worse; the 3D-cubature method is slightly better than the Taylor series expansion. Therefore, it is reasonable to model the masses in the near zone by tesseroids. In the direct surroundings of the computation point, the masses can be modelled by prisms. In the far zone, the other mass elements like the point mass, the mass line and the mass layer can be applied depending on the structure of the terrain and the computation time. The accuracy of these approaches is practically equivalent to those of the modelling by tesseroids using an analytical integration in r and Gauss–Legendre cubature (2D) ($n = m = 0$) or a Gauss–Legendre cubature (3D) ($n = m = p = 0$). The rectangular prism, which produces the most complicated formulae, needs the most computation time.

The numerical example shows that topographic and isostatic effects are significant in satellite gradiometry and could be used to smooth the satellite signal for a simplification of the downward continuation and an external calibration of the GOCE gradiometer.

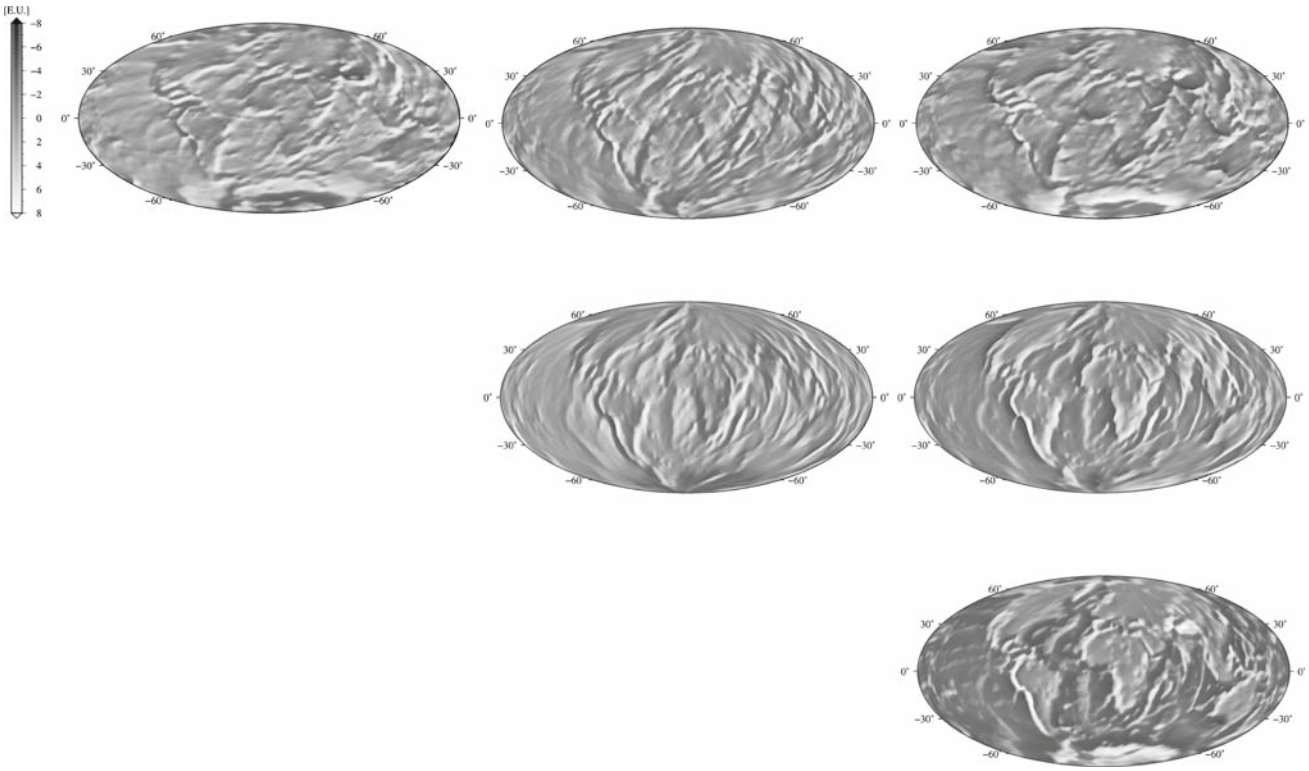

Fig. 17 Marussi tensor due to the topographic masses (Hammer projection; prime meridian: Greenwich)

Acknowledgments The support and constructive criticism of my supervisor Prof. Dr B. Heck is gratefully acknowledged. I wish to thank my colleague Dr K. Seitz for numerous discussions as well as two anonymous reviewers and the Editor-in-Chief for their valuable comments.

Appendix 1: Interpolating quadrature formulae

According to the fundamental theorem of integral calculus, the solution of a definite integral is

$$I\left(f;a,b\right)=\int_{a}^{b}f\left(x\right)\,\mathrm{d}x=F\left(b\right)-F\left(a\right),\tag{A1}$$

where $F(a)$ and $F(b)$ are the evaluations of the antiderivative of the function f at a and b, respectively. Often, only a computation by approximation of a definite integral is possible. This is the case if the antiderivative cannot be presented in closed form or the numerical evaluation is very complex. It is also possible that the function f is only known at discrete positions in the interval $[a,b]$. In the following, two methods (Schwarz 1993) concerning the computation of a definite integral by approximation are described, which are based on the approximation of the integrand by interpolation polynomials. It is possible to fix equidistant points at which the polynomial has to be evaluated (*Newton–Cotes quadrature formulae*) or to choose them in such a manner that the degree of precision is maximum (*Gauss quadrature formulae*).

A.1 Newton–Cotes quadrature formulae

The integral [Eq. (A1)] with $a=-1$, $b=1$ can be approximated by the sum

$$\tilde{I}\left(f;-1,1\right)=\sum_{i=0}^{n}w_i f\left(x_i\right),\tag{A2}$$

where x_i are denoted by "nodes" and the coefficients w_i by "weights". Fixing the integration interval to $[-1,1]$ provides no restriction, because every finite integral in $[a,b]$ can be mapped on the standard interval $[-1,1]$ using a linear transformation:

$$\tilde{I}\left(f;a,b\right)=\frac{b-a}{2}\sum_{i=0}^{n}w_i f\left(\frac{b-a}{2}x_i+\frac{a+b}{2}\right).\tag{A3}$$

For the real, in $[-1,1]$ continuous function f, $(n+1)$ pairwise different nodes $x_0,\ldots,x_n$ with $-1\le x_0<x_1<\cdots<x_n\le 1$ are given. Using these $(n+1)$ nodes and $(n+1)$ function values $f(x_i)$, $i=0,\ldots,n$, an interpolation polynomial p_n of degree smaller or equal n exists. For every polynomial $p_n\left(k\right)\in P_n\left\{p_n:p_n\left(x\right)=\sum_{i=0}^{n}\tilde{c}_i\cdot x^i;\tilde{c}_i\in\Re\right\}$,

coefficients $c_i \in \Re$ are given in the manner that p_n is obtained by

$$p_n(x) = \sum_{i=0}^{n} c_i L_i(x) \quad \text{with}$$

$$L_i(x) = \prod_{\substack{k=0 \\ k \neq i}}^{n} \frac{x - x_i}{x_k - x_i}, \quad L_i(x_k) = \delta_{ik}. \tag{A4}$$

Definition 1 The quadrature formula [Eq. (A2)] has the degree of precision n, if any polynomial up to degree n is exactly integrated, and n is the maximum possible number with this property. A quadrature formula is exact, if the integration error E is obtained by

$$E(p_n; -1, 1) := I(p_n; -1, 1) - \tilde{I}(p_n; -1, 1) = 0 \; \forall \; p_n \in P_n. \tag{A5}$$

It is possible to show the following proposition using the previous considerations.

Proposition 1 *A unique definite interpolating quadrature formula* [*Eq.* (A2)] *with degree of precision at most equal n and the weights*

$$w_i = \int_{-1}^{1} L_i(x)\, \mathrm{d}x, \quad i = 0, \ldots, n \tag{A6}$$

exists for arbitrarily given, (n+1) pairwise different nodes $x_i, i = 0, \ldots, n$ *with* $-1 \leq x_0 < x_1 < \cdots < x_n \leq 1$.

A.2 Gauss quadrature formulae

In the Newton–Cotes quadrature formulae, the nodes $x_k, k = 0, \ldots, n$ are a priori given and the associated weights w_k can be determined, resulting in the degree of precision n. In contrast, in the Gauss quadrature the nodes and the weights are chosen in such a way that the degree of precision of the quadrature formula is maximum.

Proposition 2 *The degree of precision of a quadrature formula with (n+1) nodes* x_k *and (n+1) weights* w_k *is at most 2n+1.*

Proposition 3 *There is only one quadrature formula (Eq. A2) with (n+1) nodes* x_i *which has the degree of precision 2n+1. The nodes* x_i *are the zero points of the Legendre polynomial* $P_{n+1}(x)$ *of degree (n+1) (Bronstein 1997):*

$$P_m(x) = \frac{1}{2^m m!} \frac{\mathrm{d}^m}{\mathrm{d}x^m} \left(x^2 - 1\right)^m, \quad m \in N_0. \tag{A7}$$

The weights are defined as

$$w_i = \int_{-1}^{1} \prod_{\substack{i=0 \\ i \neq k}}^{n} \left(\frac{x - x_i}{x_k - x_i}\right)^2 \mathrm{d}x > 0. \tag{A8}$$

Table 4 Values of the nodes and weights of the Gauss–Legendre quadrature formulae for $0 \leq n \leq 5$

n	$x_i, i = 0 \ldots n$	$w_i, i = 0 \ldots n$
0	0.0000000000 0000000000	2.0000000000 0000000000
1	0.5773502691 8962576451	1.0000000000 0000000000
	−0.5773502691 8962576451	1.0000000000 0000000000
2	0.7745966692 4148337704	0.5555555555 5555555556
	0.0000000000 0000000000	0.8888888888 8888888889
	−0.7745966692 4148337704	0.5555555555 5555555556
3	0.8611363115 9405257523	0.3478548451 3745385737
	0.3399810435 8485626480	0.6521451548 6254614263
	−0.3399810435 8485626480	0.6521451548 6254614263
	−0.8611363115 9405257523	0.3478548451 3745385737
4	0.9061798459 3866399280	0.2369268850 5618908751
	0.5384693101 0568309104	0.4786286704 9936646804
	0.0000000000 0000000000	0.5688888888 8888888889
	−0.5384693101 0568309104	0.4786286704 9936646804
	−0.9061798459 3866399280	0.2369268850 5618908751
5	0.9324695142 0315202781	0.1713244923 7917034504
	0.6612093864 6626451366	0.3607615730 4813860757
	0.2386191860 8319690863	0.4679139345 7269104739
	−0.2386191860 8319690863	0.4679139345 7269104739
	−0.6612093864 6626451366	0.3607615730 4813860757
	−0.9324695142 0315202781	0.1713244923 7917034504

The proofs of Propositions 1 to 3 are presented in Schwarz (1993). The position of the nodes and the related weights for polynomial degree up to 5 are tabulated, e.g., in Engeln-Müllges and Reutter (1987) or Faires and Burden (2003) and up to polynomial degree 16 in Stroud (1974). Table 4 summarizes the values of the nodes x_i and the weights w_i for the Gauss–Legendre quadrature formulae up to $n = 5$.

A3 Gauss–Legendre cubature of surface integrals (2D)

In 2D, the unit square $[-1, 1] \times [-1, 1]$ is the widely used standard domain where all the 2D integration domains can be traced back using an affine transformation. A frequently used method for the numerical integration over such a unit square is the consideration of the integral as a 2D iterated integral and the application of a quadrature formula for each integration variable. The formulae that result from this way of computation are called "(Cartesian) product formulae" (e.g., Burden and Faires 1993; Klees 1992; Stroud 1974). Based on the double integral over the surface element F

$$\iint_F f(x, y)\, \mathrm{d}x\mathrm{d}y = \int_a^b \left(\int_c^d f(x, y)\, \mathrm{d}y \right) \mathrm{d}x, \text{ where } F = \{(x, y) |\, a \leq x \leq b, c \leq y \leq d\} \tag{A9}$$

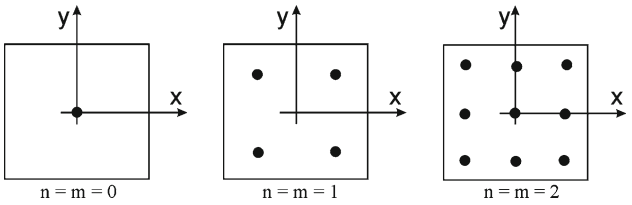

Fig. 18 Position of the nodes for Gauss–Legendre product formulae (2D)

the approximation using a transformation from the rectangle F to the unit square is

$$\int_{-1}^{1}\int_{-1}^{1} f\,(x,y)\;\mathrm{d}x\mathrm{d}y = \sum_{i=0}^{n}\sum_{j=0}^{m} w_i w_j f\left(x_i, y_j\right). \tag{A10}$$

The position of the nodes up to degree of precision 3 (see Definition 1) is shown in Fig. 18.

It can be recognized that $(n+1)\cdot(m+1)$ nodes result for the degrees $(2n+1)$, $(2m+1)$ of precision in the respective coordinate directions. For higher degrees n, m the number of evaluations of the integral kernel may be rather large. As a consequence, this procedure may be highly time consuming, in particular when the functions are as complicated as the integral kernels derived in Sect. 2.1.3. The 2D spherical integrals $\iint_{\sigma} f\left(\varphi', \lambda'\right)\,\mathrm{d}\sigma$ take the form

$$\begin{aligned}&\int_{\varphi_1'}^{\varphi_2'}\int_{\lambda_1'}^{\lambda_2'} f\left(\varphi', \lambda'\right)\cos\varphi'\mathrm{d}\varphi'\mathrm{d}\lambda' \\ &= \int_{\lambda_1'}^{\lambda_2'}\left(\int_{\varphi_1'}^{\varphi_2'} f\left(\varphi', \lambda'\right)\cos\varphi'\mathrm{d}\varphi'\right)\mathrm{d}\lambda'.\end{aligned} \tag{A11}$$

A.4 Gauss–Legendre cubature of volume integrals (3D)

Analogously to the solution of the 2D surface integral, the 3D-integral over the volume element V

$$\begin{aligned}&\iiint_V f\,(x,y,z)\;\mathrm{d}x\,\mathrm{d}y\,\mathrm{d}z \\ &= \int_a^b\left(\int_c^d\left(\int_e^f f\,(x,y,z)\;\mathrm{d}z\right)\mathrm{d}y\right)\mathrm{d}x,\end{aligned} \tag{A12a}$$

$$V = \{(x,y,z)|\; a \le x \le b, c \le y \le d, e \le z \le f\} \tag{A12b}$$

can be approximated by means of a transformation per coordinate direction from the unit cube

$$\begin{aligned}&\int_{-1}^{1}\int_{-1}^{1}\int_{-1}^{1} f\,(x,y,z)\,\mathrm{d}x\,\mathrm{d}y\,\mathrm{d}z \\ &= \sum_{i=0}^{n}\sum_{j=0}^{m}\sum_{k=0}^{p} w_i w_j w_k f\left(x_i, y_j, z_k\right).\end{aligned} \tag{A13}$$

An algorithm for the numerical solution of the triple integral via Gauss–Legendre cubature (3D) can be found in Ardalan and Safari (2004) or Burden and Faires (1993). The position of the nodes is illustrated in Fig. 19; the number increases with nmp depending on the degree of precision.

Although the number of nodes, and the number of function evaluations, may be much larger for the numerical evaluation of triple integrals, the total numerical effort can be significantly smaller than in the case of the 2D cubature, depending on the complexity of the integral kernels. In particular, this property holds for the kernels related to the tesseroid potential and its derivatives. The 3D integral of the potential and its derivatives (see Sect. 2.1.1) can be expressed as

$$\begin{aligned}&\iiint_{\Omega} f\left(\xi, \varphi', \lambda'\right)\mathrm{d}\Omega \\ &= \int_{\xi_1}^{\xi_2}\int_{\varphi_1'}^{\varphi_2'}\int_{\lambda_1'}^{\lambda_2'} f\left(\xi, \varphi', \lambda'\right)\xi^2\cos\varphi'\mathrm{d}\lambda'\mathrm{d}\varphi'\mathrm{d}\xi \\ &= \int_{\xi_1}^{\xi_2}\left(\int_{\varphi_1'}^{\varphi_2'}\left(\int_{\lambda_1'}^{\lambda_2'} f\left(\xi, \varphi', \lambda'\right)\mathrm{d}\lambda'\right)\cos\varphi'\mathrm{d}\varphi'\right)\xi^2\mathrm{d}\xi.\end{aligned} \tag{A14}$$

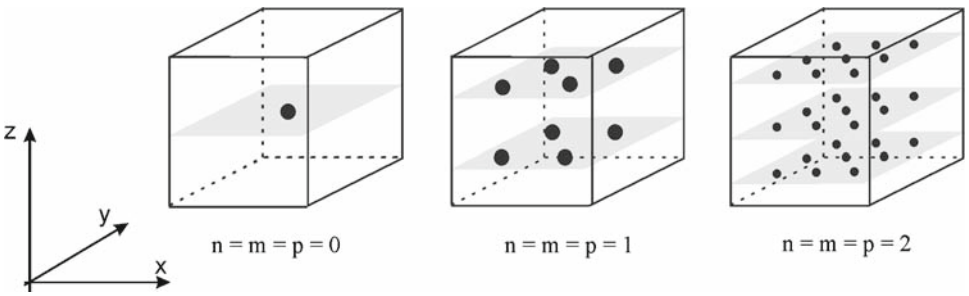

Fig. 19 Position of the nodes for Gauss–Legendre product formulae (3D)

References

Anderson EG (1976) The effect of topography on solutions of Stokes' problem. Rep Unisurv S-14, School of Surveying, University of New South Wales, Kensington

Ardalan AA, Safari A (2004) Ellipsoidal terrain correction based on multi-cylindrical equal-area map projection of the reference ellipsoid. J Geod 78(1–2):114–123. doi:10.1007/s00190-004-0381-6

Blakely RJ (1995) Potential theory in gravity and magnetic applications p 441. Cambridge University Press, New York

Bouman J, Koop R (2003) Geodetic methods for calibration of GRACE and GOCE. Space Sci Rev 108: 293–303

Bronstein IN (1997) Taschenbuch der Mathematik. Verlag Harri Deutsch, Frankfurt am Main

Burden RL, Faires JD (1993) Numerical analysis, Fifth edn. PWS Publishing Company, Boston

Denker H (2006) Das Europäische Schwere- und Geoidprojekt (EGGP) der Internationalen Assoziation für Geodäsie. Z.f. Verm.wesen 131: 335–344

Engeln-Müllges G, Reutter F (1987) Numerische Mathematik für Ingenieure.. BI Wissenschaftsverlag, Zürich

Faires D, Burden R (2003) Numerical methods. Third edn. Thomson Brooks/Cole, Pacific Grove

Forsberg R (1984) A study of terrain reductions , density anomalies and geophysical inversion methods in gravity field modelling. Rep 355, Department of Geodetic Science, The Ohio State University, Columbus

Forsberg R, Tscherning CC (1997) Topographic effects in gravity modelling for BVP. In: Sansò F, Rummel R (eds) Geodetic boundary value problems in view of the one centimetre geoid. Lecture notes in earth sciences, vol. 65. Springer, Berlin pp 241–272

Grüninger W (1990) Zur topographisch-isostatischen Reduktion der Schwere. PhD thesis, Universität Karlsruhe

Heck B (2003) On Helmert's methods of condensation. J Geod 77(3–4): 155–170. doi:10.1007/s00190-003-0318-5

Heck B, Wild F (2005) Topographic reductions in satellite gravity gradiometry based on a generalized condensation model. In: Sansò F (ed) A window on the future of geodesy.. Springer, Berlin pp 294–299

Heck B, Seitz K (2007) A comparison of the tesseroid, prism and point-mass approaches for mass reductions in gravity field modelling. J Geod 81(2):121–136. doi:10.1007/s00190-006-0094-0

Janák J, Mikula K, Šprlák M (2007) Downward continuation of satellite gradiometric data. Proc. of the third international GOCE user workshop, ESA-ESRIN, Frascati, Italy, 6–8 November 2006 (ESA SP-627, January 2007), CD-Rom

Klees R (1992) Lösung des fixen geodätischen Randwertproblems mit Hilfe der Randelementmethode. Reihe C, Heft Nr. 382, Deutsche Geodätische Kommission, München

Koop R, Visser P, Tscherning C (2001) Aspects of GOCE calibration. International GOCE user workshop, vol. WPP-1888, pp 51–56

Kuhn M (2000) Geoidbestimmung unter Verwendung verschiedener Dichtehypothesen. Reihe C, Heft Nr. 520. Deutsche Geodätische Kommission, München

Kühtreiber N, Kraiger G, Meurers B (1989) Pilotstudien für eine Bouguer-Karte von Österreich. In: Lichtenegger H, Steinhauser P, Sünkel H (eds) Tagungsbericht über das 5. internationale Alpengravimetrie-Kolloquium. Österreichische Beiträge zu Meteorologie und Geophysik, Heft 2, S. 51–71, Wien

Mader K (1951) Das Newtonsche Raumpotential prismatischer Körper und seine Ableitungen bis zur dritten Ordnung. Österreichische Zeitschrift für Vermessungswesen Sonderheft 11, Österreichischer Verein für Vermessungswesen

Makhloof A, Ilk KH (2005) Far-zone topography effects on gravity and geoid heights according to Helmert's methods of condensation and based on Airy-Heiskanen model. Proc. third Minia int. conf. for advanced trends in engineering

MAPLE (2003) Maplesoft, Version 9.03. Source http://www.maplesoft.com/

Martinec Z (1998) Boundary-value problems for gravimetric determination of a precise geoid. Lecture notes in earth sciences 73. Springer, Berlin

Nagy D (1966) The gravitational attraction of a right rectangular prism. Geophysics 31(2): 362–371

Nagy D, Papp G, Benedek J (2000) The gravitational potential and its derivatives for the prism. J Geod 74(7–8):552–560. doi:10.1007/s001900000116

Nagy D, Papp G, Benedek J (2002) Corrections to "The gravitational potential and its derivatives for the prism". J Geod 76(8):475 doi:10.1007/s00190-002-0264-7

Novák P (2000) Evaluation of gravity data for the Stokes-Helmert solution of the geodetic boundary value problem. PhD Dissertation, Technical report of the Department of Geodesy and Geomatics Engineering, 207, University of New Brunswick, Fredericton

Novák P, Vaníček P, Martinec Z, Véronneau M (2001) Effects of the spherical terrain on gravity and the geoid. J Geod 75:691–706. doi:10.1007/s00190-005-0435-4

Novák P, Grafarend EW (2005) Ellipsoidal representation of the topographical potential and its vertical gradient. J Geod 78(11–12):691–706. doi:10.1007/s00190-005-0435-4

Schwarz HR (1993) Numerische Mathematik. Teubner Verlag, Stuttgart

Stroud AH (1974) Numerical quadrature and solution of ordinary differential equations. Springer, Berlin

Tscherning CC (1976) Computation of the second-order derivatives of the normal potential based on the representation by a Legendre series.. manuscripta geodaetica 1(1): 71–92

Tsoulis D (1999) Analytical and numerical methods in gravity field modelling of ideal and real masses. Reihe C, Heft Nr 510, Deutsche Geodätische Kommission, München

Vaníček P, Novák P, Martinec Z (2001) Geoid, topography, and the Bouguer plate or shell. J Geod 75(4):210–215. doi:10.1007/s001900100165

Vaníček P, Tenzer R, Sjoberg LE, Martinec Z, Featherstone WE (2004) New views of the spherical Bouguer gravity anomaly. Geophys J Int 159(2): 460–472

Wild F, Heck B (2004) Effects of topographic and isostatic masses in satellite gravity gradiometry. Proc. second international GOCE user workshop *GOCE*, The Geoid and Oceanography, ESA-ESRIN, (ESA SP – 569, June 2004), CD-ROM

Wild F, Heck B (2005) A comparison of different isostatic models applied to satellite gravity gradiometry. In: Jekeli C, Bastos L, Fernandes J (eds) Gravity, geoid and space missions. Springer, Berlin pp 230–235

Wild-Pfeiffer F, Heck B (2006) Topographic and isostatic reductions for use in satellite gravity gradiometry. VI Hotine-Marussi symposium of theoretical and computational geodesy: challenge and role of modern geodesy, Wuhan, May 29 – June 2, 2006, in press

Wild-Pfeiffer F (2007) Auswirkungen topographisch-isostatischer Effekte auf die Satellitengradiometrie. Reihe C, Heft Nr 604, Deutsche Geodätische Kommission, München